

MPP-2021-134
JLAB-PHY-21-3487
November 15, 2021

Deeply Learning Deep Inelastic Scattering Kinematics

Markus Diefenthaler^{1a}, Abduhhal Farhat^{2b}, Andrii Verbytskyi^{3c}
and
Yuesheng Xu^{4b}

^aThomas Jefferson National Accelerator Facility, Newport News, VA 23606, USA

^bDepartment of Mathematics & Statistics, Old Dominion University, Norfolk, VA 23529, USA

^cMax-Planck-Institut für Physik, D-80805 Munich, Germany

Abstract

We study the use of deep learning techniques to reconstruct the kinematics of the deep inelastic scattering (DIS) process in electron-proton collisions. In particular, we use simulated data from the ZEUS experiment at the HERA accelerator facility, and train deep neural networks to reconstruct the kinematic variables Q^2 and x . Our approach is based on the information used in the classical reconstruction methods, the measurements of the scattered lepton, and the hadronic final state in the detector, but is enhanced through correlations and patterns revealed with the simulated data sets. We show that, with the appropriate selection of a training set, the neural networks sufficiently surpass all classical reconstruction methods on most of the kinematic range considered. Rapid access to large samples of simulated data and the ability of neural networks to effectively extract information from large data sets, both suggest that deep learning techniques to reconstruct DIS kinematics can serve as a rigorous method to combine and outperform the classical reconstruction methods.

¹ mdiefent@jlab.org

² afarh002@odu.edu

³ andrii.verbytskyi@mpp.mpg.de

⁴ y1xu@odu.edu

1 Introduction

Studies by a multitude of deep-inelastic scattering (DIS) experiments all over the world have revealed information on the quark-gluon structure of nuclear matter and established quantum chromodynamics (QCD) as the theory of the strong interaction [1–3].

The experiments at the HERA collider facility at the DESY research center in Hamburg, Germany have played an important role in these studies. HERA has been the only electron-proton collider built so far [4]. The data collected in the years 1992 - 2007 have provided truly unique information on the internal structure of the proton and other hadrons [5].

The key component in these studies has been a precise reconstruction of DIS kinematics, using information from the accelerator and the detectors. Multiple methods have been applied at the HERA experiments [6] to reach an optimal precision in each particular measurement. Each of the classical reconstruction methods uses only partial information from the DIS event and is subject to specific limitations, either arising from the detector or the assumptions used in the method.

With the DIS measurements at the upcoming Electron-Ion Collider in mind [7], we present in this work a novel method for the reconstruction of DIS kinematics based on supervised machine learning and study its performance using data from the ZEUS experiment [8] at HERA. For our approach, we develop deep neural network (DNN) models that are optimized for the problem and allow to take the full information from the DIS event into account. We train the DNN models on simulated data from the ZEUS experiment and compare the results from our trained model with the results from the classical reconstruction methods.

We show that the reconstruction of the DIS kinematics using deep neural networks provides a rigorous, data-driven method to combine and outperforms classical reconstruction methods over a wide kinematic range. In the past, neural networks have already been used in the context of DIS experiments [9] and we expect that our novel method and similar approaches will play an even more important role in ongoing and future DIS experiments [10, 11].

2 Deep inelastic scattering

Deep inelastic scattering is a process in which a high-energy lepton (l) scatters off a nucleon or nucleus target (h) with large momentum transfer (the momentum of each

entity is given in parenthesis):

$$l(\vec{k}) + h(\vec{P}) \rightarrow l'(\vec{k}') + \mathcal{H}(\vec{P}'). \quad (1)$$

The detectors in collider experiments are designed to measure the final state of the DIS process, consisting of the scattered lepton l' and the hadronic final state \mathcal{H} . The latter consists of hadrons with a relatively long lifetime as well as some photons and leptons. The H1 and ZEUS experiments were not able to register the remnant of the target due to its proximity to the proton beam pipe.

2.1 Deep inelastic scattering at Born level

In the leading order (Born) approximation, the leptons interact with hadrons by the exchange of a single virtual γ or Z boson in the neutral current (NC) reaction, and the exchange of single W^\pm boson in the charged current (CC) reaction. The kinematics of the leading order DIS process in a Feynman diagram-like form is shown in Fig. 1. In this

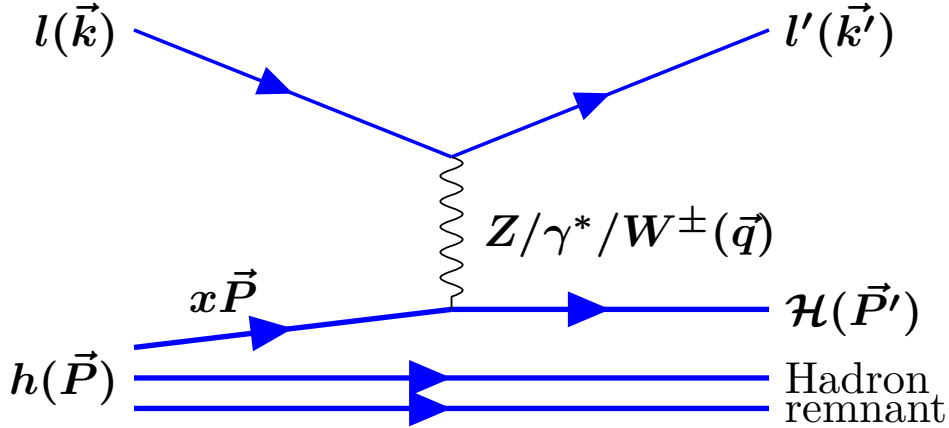


Figure 1: Schematic representation of Deep Inelastic Scattering process at Born level.

paper, we will consider the neutral current electron scattering off a proton in a collider experiment. In this reaction, the final state lepton is a charged particle (electron or positron) that can be easily registered and identified in the detector.

With a fixed center-of-mass energy, $\sqrt{s} = \sqrt{(\vec{k} + \vec{P})^2}$, two independent, Lorentz-invariant, scalar quantities are sufficient to describe the deep inelastic scattering event kinematics in Born approximation. Typically, the used quantities are:

- the four-momentum transferred to the hadronic system

$$Q^2 = -\vec{q} \cdot \vec{q} = -(\vec{k} - \vec{k}')^2, \quad (2)$$

- the Bjorken scaling variable, interpreted in the frame of a fast moving nucleon as the fraction of incoming nucleon longitudinal momentum carried by the struck parton:

$$x = \frac{Q^2}{2\vec{P} \cdot \vec{q}}. \quad (3)$$

In addition to that, the inelasticity y is used to define the kinematic region of interest. It is defined as the fraction of incoming electron energy taken by the exchanged boson

$$y = \frac{\vec{P} \cdot \vec{q}}{\vec{P} \cdot \vec{k}}. \quad (4)$$

However, the Born-level picture of the DIS process is not sufficient for the description of the observed physics phenomena. A realistic description of the DIS process requires an inclusion of higher order QCD and QED corrections [12].

2.2 Higher order corrections to deep-inelastic scattering process

The DIS process with leading order QED corrections can be written as

$$l(\vec{k}) + h(\vec{P}) \rightarrow l'(\vec{k}') + \gamma(\vec{P}_\gamma) + X(\vec{P}'), \quad (5)$$

so the kinematics is defined not only with the kinematic of the scattered electron and the struck parton, but also with the momentum of the radiated γ , \vec{P}_γ . The lowest order QED radiative corrections can be depicted in a form of Feynman diagrams as shown in Fig. 2 a)-d) and should be considered together with the virtual corrections e)-g). The Fig. 2 a),d) correspond to the initial state radiation (ISR) and the Fig. 2 b),c) to the final state radiation (FSR).

With the virtual corrections taken into account in the DIS process, Eq. 2 no longer holds, i.e.

$$\vec{q} \cdot \vec{q} \neq -(\vec{k} - \vec{k}')^2. \quad (6)$$

The presence of higher order QCD corrections makes the kinematic description of the DIS process even more complicated. Therefore, the exact definitions of the kinematic observables used in every measurement in the DIS process and the corresponding simulations are essential for the correct physics interpretation.

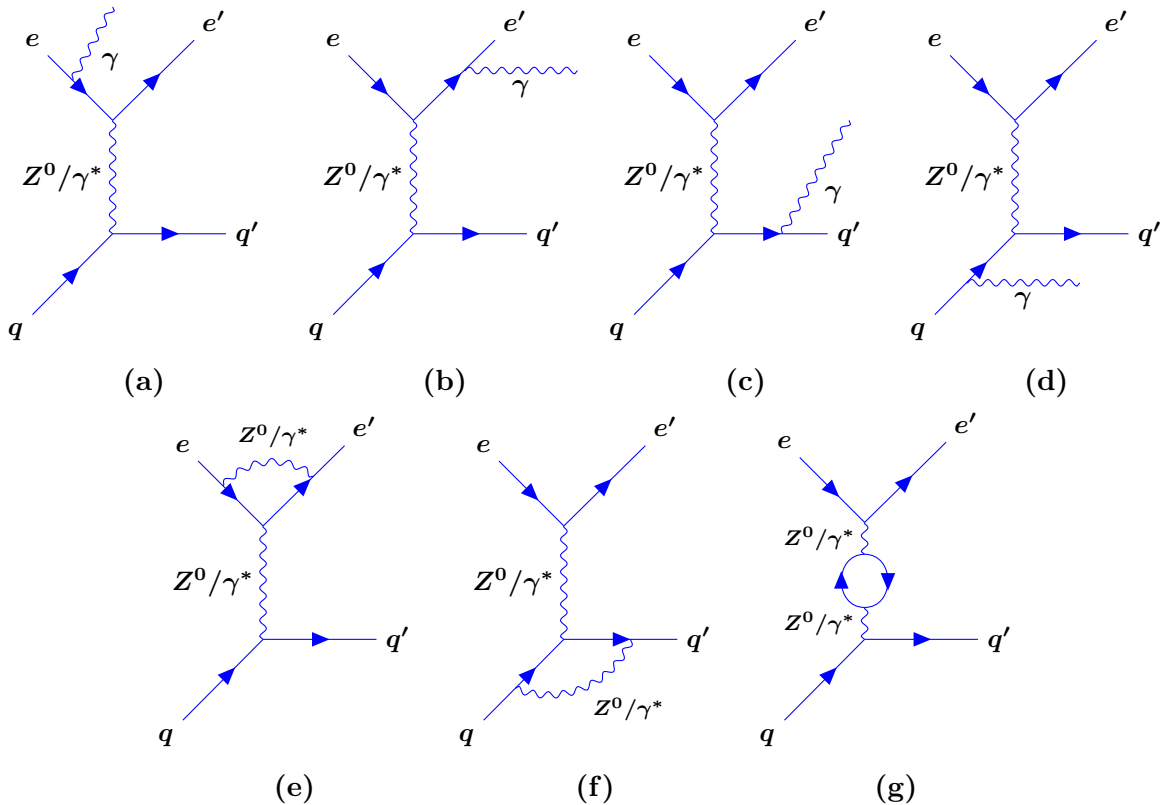


Figure 2: *Feynman diagrams for Deep Inelastic Scattering process with some leading order electroweak corrections.*

2.3 The simulation of the DIS events and the kinematic variables in the simulated events

The simulation of the inclusive DIS events in the Monte Carlo event generators (MCEGs) starts from the simulation at the parton level, i.e. the simulation of the hard scattering process and the kinematics of the involved partons. The later starts from the modeling of the partonic content of the hadron using the parton density functions (PDFs) [13] for the given hadron and considering processes with all combinations of partons in the initial state. This modeling combines the calculations of the perturbative QED and/or QCD matrix elements for the $2 \rightarrow n$ processes on parton level with the different QCD parton cascade algorithms aimed to take into account at least some parts of the higher order perturbative QCD corrections not present in the calculations of matrix elements.

The simulated collision events on the particle (hadron) level are obtained using the parton level simulations as input and applying phenomenological hadronization and particle decay models to them.

As of 2021, multiple MCEG programs are capable of simulating the inclusive DIS process

at the hadron level with different levels of precision and sophistication, e.g. `Pythia6` [14], `Pythia8` [15], `SHERPA-MC` [16], `WHIZARD` [17] and `Herwig7` [18]. In addition to that, `Lepto` [19], `Ariadne` [20], `Cascade` [21] and `Rapgap` [22] programs can simulate the DIS process using parts of the `Pythia6` framework for the simulation of hadronization processes and decays of particles.

As it was discussed above, DIS beyond the Born approximation has a complicated structure which involves the QCD and QED corrections. The most recent MCEG programs, e.g., `Herwig7`, `Pythia8`, `SHERPA-MC`, or `WHIZARD`, implement these corrections in their own frameworks or are able to use the specialized packages like `OpenLoops` [23], `blackhat` [24] or `MadGraph` [25]. In general, the modern MCEGs do not provide their definitions of the DIS kinematic observables, but in some cases those can be calculated from the kinematics of the initial and final state partons at the parton level. For instance, under some assumptions the Q^2 in the event could be calculated according to Eq. 2. The total elimination of the ambiguities for such calculations is not possible, as the final state kinematics even at the parton level depends not only on the hard process kinematics but also on the subsequent hard and soft QCD or QED radiation. The calculations of the kinematic observables from the momenta of particles at hadron level add an additional ambiguity related to the identification of the scattered lepton and the distinction of that lepton from the leptons produced in the hadronization and decay processes.

Contrary to the approach used in the modern MCEGs, the MCEGs contemporary to HERA experiments relied on the case-by-case implementation of the higher order corrections beyond the Born approximation (e.g. `Rapgap` [22]) or used `HERACLES` [12] for the higher order QED and QCD corrections. Some of these programs provided specific definitions of the DIS kinematic observables taking or not taking the radiative corrections into account. In this way all the ambiguities related to the determination of the kinematic observables are contained in these specific definitions.

The way to get a simulation of the DIS collision even in a specific detector is the same as for any other type of particle collision event. It involves simulation of the particle transport through the detector material, simulation of detector response and is typically performed in `Geant` [26, 27] or similar tools. The simulated detector response is passed to the experiment-specific reconstruction programs and should be indistinguishable from the real data recorded by the detector and processed in the same way.

2.4 Reconstruction of the kinematic variables at the detector level

The kinematics of the DIS events are reconstructed in the collider experiment by identifying and measuring the momentum of the scattered lepton l' and/or the measurements of the hadronic final state (\mathcal{H}). The identification of the scattered lepton is ambiguous even at the particle level of the simulated DIS collision events. The same ambiguity is present in the reconstructed real and simulated data at the detector level. Therefore, the identification of the scattered electron candidate for the purposes of physics analyses is a complicated task on itself and was a subject of multiple studies in the past, some of which also involved the neural network-related techniques [9]. In our paper, we rely on the standard method of the electron identification at the ZEUS experiment (ZEUS) and discuss solely the reconstruction of the kinematic variables using the identified electron and other measured quantities.

The physics analyses performed in the experiments at HERA revealed that the following quantities could provide information for the calculations of the kinematic observables:

- The energy (E_{ν}) and polar angle (θ_{ν}) of the scattered electron. Most of the DIS experiments are equipped to register the scattered electron using the tracking and calorimeter detector subsystems. While the tracking system is able to provide the information on the momentum of the scattered electron, the calorimeter system can be used to estimate the energy of the electron and the total energy of the collinear radiation emitted by the electron. At the detector level, the estimation of these energies can be done by comparing the momentum of the electron reconstructed in the tracking system and the energy deposits registered in the calorimeter system around the extrapolated path of the electron in the calorimeter.
- The energy of the HFS expressed in terms of the following convenient variables:

$$\delta_{\mathcal{H}} = \sum_{i \in \mathcal{H}} E_i - P_{Z,i} \quad (7)$$

and

$$P_{T,\mathcal{H}} = \sqrt{\left(\sum_{i \in \mathcal{H}} P_{X,i}\right)^2 + \left(\sum_{i \in \mathcal{H}} P_{Y,i}\right)^2}, \quad (8)$$

where the sums run over the registered objects i excluding the scattered electron. Depending on the analysis requirements, the used objects could be either registered tracks, energy deposits in the calorimeter system, or a combination of both.

The measurements of the quantities listed above overconstrain the reconstruction of the

event kinematics. Therefore, in the simplest case, any subset of two observables in E_ν , θ_ν , $\delta_{\mathcal{H}}$, and $P_{T,\mathcal{H}}$, can be used for the reconstruction.

In our analysis we consider three specific classical reconstruction methods based on these observables which were used by the ZEUS collaboration in the past: the electron, the Jacques-Blondel, and the double-angle methods. We briefly provide some details on the methods in this section, while a more detailed description can be found elsewhere [28].

The electron (EL) method uses only measurements of the scattered lepton, E_ν and θ_ν , to do the reconstruction. The kinematic variables calculated from these measurements are given by:

$$Q_{EL}^2 = 2E_l E_\nu (1 + \cos \theta_\nu) \quad (9)$$

and

$$x_{EL} = \frac{E_\nu (1 + \cos \theta_\nu)}{2E_P (E_l - E_\nu (1 + \cos \theta_\nu))}. \quad (10)$$

The electron method provides a precise reconstruction of kinematics, but, since it uses only information from the scattered lepton, this method is affected by initial and final state QED radiation. Namely, the QED radiation registered in the detector separately from the scattered electron will not be taken into account in the calculations with this method. Practically, the reconstruction with this method gives reasonable results when E_l and E_ν are significantly different from one another, but the resolution and stability becomes poor otherwise.

The Jacques-Blondel (JB) method uses only measurements of the final state hadronic system, $\delta_{\mathcal{H}}$ and $P_{T,\mathcal{H}}$, for the reconstruction. The kinematic variables are calculated from these by:

$$Q_{JB}^2 = \frac{2E_l P_{T,\mathcal{H}}^2}{2E_l - \delta_{\mathcal{H}}}, \quad (11)$$

$$x_{JB} = \frac{2E_l Q_{JB}^2}{s \delta_{\mathcal{H}}}. \quad (12)$$

The Jacques-Blondel method reconstructs the DIS kinematic variables using only information measured from the HFS. This makes the method resistant to possible biases because of unaccounted QED FSR, but requires precise measurements of the particles momenta in the hadronic final state. The factors that limit the precision of the measurements are the particle identification precision, limited resolution of the tracking and calorimeter systems, impossibility of the particle detection around the beampipe and presence of objects that avoid detection (e.g. neutrinos from the particle decays).

The double-angle (DA) method combines measurements from the scattered lepton and the final-state hadronic system, θ_ν and $\gamma_{\mathcal{H}}$, to perform the kinematic reconstruction as

follows:

$$Q_{DA}^2 = \frac{4E_l^2 \sin \gamma_{\mathcal{H}}(1 + \cos \theta_{l'})}{\sin \gamma_{\mathcal{H}}(1 - \cos \theta_{l'})}, \quad (13)$$

$$x_{DA} = \frac{E_l \sin \gamma_{\mathcal{H}}(1 + \cos \theta_{l'})}{E_P \sin \theta_{l'}(1 - \cos \gamma_{\mathcal{H}})}, \quad (14)$$

where the angle $\gamma_{\mathcal{H}}$ is defined as

$$\cos \gamma_{\mathcal{H}} = \frac{P_{T,\mathcal{H}}^2 - \delta_{\mathcal{H}}^2}{P_{T,\mathcal{H}}^2 + \delta_{\mathcal{H}}^2}. \quad (15)$$

The angle $\gamma_{\mathcal{H}}$ depends on the ratio of the measured quantities $\delta_{\mathcal{H}}$ and $P_{T,\mathcal{H}}$, thus, uncertainties in the hadronic energy measurement tend to cancel, leading to good stability of the reconstructed kinematic variables. Similar to the electron method, when E_l and $E_{l'}$ are significantly different from one another, the double-angle method provides reliable results, but the resolution and stability are poor otherwise.

2.5 The methodology of measurements in the deep inelastic ep collisions

The methodology of measurements at lepton-hadron colliders in general is similar to the methodologies used at e^+e^- and hadron-hadron colliders. Briefly, in the most cases the quantity of interest gets measured from the real data registered in the detector corrected for detector effects. The corrections are estimated by comparing the analysis at the detector level with the same analysis at particle level using detailed simulations of the collision events.

The main difference between the measurements at lepton-hadron colliders and elsewhere, is in the way the measurements involve collision kinematics. At e^+e^- colliders, the initial kinematics of the interactions is given by the lepton energies that are known parameters of the accelerators. Therefore, it is straightforward for most of the measurements in the e^+e^- experiments to estimate the center-of-mass energy of the hard collision process. In hadron-hadron collider experiments, there is no way to measure the kinematic properties of the partons initiating the collision process, as the involved partons cannot be observed in a free state and most measurements in the hadron-hadron collisions are inclusive in the kinematics of the initial state. The DIS collisions at electron-proton colliders take a middle stance between these cases. The kinematic observables of the DIS process are measured on an event-by-event basis at the detector level using the methods described above. For a proper comparison of the measurements of HFS to corresponding pQCD predictions, the detector-level measurements are corrected for detector effects as well as

ISR and FSR QED effects using MCEGs or specialized programs [29]. The correction procedures could vary depending on the quantities measured and the used definitions of the kinematic observables at the particle level. Therefore, in this analysis, to keep the corrections for ISR and FSR QED effects out of scope, at particle-level we use a single definition of “true” kinematic observables that is based on the kinematics of the exchanged boson.

Namely, we use the definitions of the true-level observables Q_{true}^2 and x_{true} that follow the definitions implemented in ZEUS Common NTuples [30,31] and were used in many ZEUS analyses. With these definitions the Q_{true}^2 is calculated directly from the four-momentum of the exchange boson \vec{q}_{boson} ,

$$Q_{\text{true}}^2 = -|\vec{q}_{\text{boson}}|^2. \quad (16)$$

The x_{true} is calculated according to the formula

$$x_{\text{true}} = \frac{Q_{\text{true}}^2}{y_{\text{after ISR}} s_{\text{after ISR}}}, \quad (17)$$

with

$$y_{\text{after ISR}} = \frac{\vec{q}_{\text{boson}} \cdot \vec{P}_{\text{proton beam}}}{(\vec{P}_{\text{lepton beam}} - \vec{P}_{\text{ISR radiation}}) \cdot \vec{P}_{\text{proton beam}}} \quad (18)$$

and

$$s_{\text{after ISR}} = |\vec{P}_{\text{proton beam}} + \vec{P}_{\text{lepton beam}} - \vec{P}_{\text{ISR radiation}}|^2, \quad (19)$$

where $\vec{P}_{\text{proton beam}}$, $\vec{P}_{\text{lepton beam}}$ and $\vec{P}_{\text{ISR radiation}}$ represent the four-momenta of the proton beam particles, lepton beam particles and the momenta lost by the lepton beam particles to ISR. Thus, $y_{\text{after ISR}}$ corresponds to the fraction of energy of the bare lepton (i.e. without the ISR) transferred to the HFS in the center of mass of the proton and $s_{\text{after ISR}}$ to the center of mass-energy squared of the proton and the incoming bare electron.

3 Machine learning methods

The reconstruction of DIS event kinematics is overconstrained by the previously mentioned measurements, $E_{l'}$, $\theta_{l'}$, $\delta_{\mathcal{H}}$, and $P_{T,\mathcal{H}}$. We trained an ensemble of deep neural networks (DNNs) to reconstruct x and Q^2 by correcting results from classical reconstruction methods using the information on the scattered lepton and the final-state hadronic system.

The ensemble DNN method presented here is a new approach designed specifically to address this reconstruction problem. The remainder of this section discusses in detail specifics of the DNN architectures, the specific optimization methods used to find the

optimal parameters defining the DNNs, and the specific structure of the ensemble models. Shown rigorously in what follows, the main justification for using the unique model is:

- the universal approximation capabilities of the DNN models with our specific architectures
- the necessary reduction in the approximation error with the increase in the depth of our DNN models
- avoidance of a degradation problem [32] in training due to residual structure of our DNN models.

Further details on the DNN-based reconstruction method will be provided in Ref. [33].

3.1 Neural networks are universal approximators

The problem of reconstruction of DIS event kinematics can be posed as task to construct a functional relationship between a set of input variables \mathbf{x} and a set of response variables y . In many cases, such a relation is a continuous function, and can be approximated to arbitrary accuracy with a neural network. The corresponding neural network can have various architectures. The simplest architecture is a sequence of fully-connected, feed-forward (hidden) layers. For an input $\mathbf{x} \in \mathbb{R}^m$, the output of the first hidden layer is:

$$h^1(\mathbf{x}) = \alpha(A_0\mathbf{x}), \quad h^1 \in \mathbb{R}^{d_1}, \quad (20)$$

where $A_0 : \mathbb{R}^m \rightarrow \mathbb{R}^{d_1}$ is an affine transformation, the composition of a translation and a linear mapping, and $\alpha : \mathbb{R} \rightarrow \mathbb{R}$ is a nonlinear function, called an activation function. Define the application of α on a vector $\mathbf{x} := (x_1, x_2, \dots, x_m)^T \in \mathbb{R}^m$, by $\alpha(\mathbf{x}) := (\alpha(x_1), \alpha(x_2), \dots, \alpha(x_m))^T$.

For $A_1 : \mathbb{R}^{d_1} \rightarrow \mathbb{R}^{d_2}$, the output h^1 is passed into a second hidden layer:

$$h^2(\mathbf{x}) = \alpha(A_1 h^1(\mathbf{x})), \quad h^1 \in \mathbb{R}^{d_2}, \quad (21)$$

and so on, for a desired number of hidden layers. An affine transformation on the output of the final hidden layer is the output of the network. For $i \in \mathbb{N}$, call d_i the number of nodes in hidden layer i .

Define $\Psi_{m,n}^D(\alpha)$ to be the set of neural networks with D hidden layers that map $\mathbb{R}^m \rightarrow \mathbb{R}^n$ with continuous, nonlinear activation function α . If $\psi \in \Psi_{m,n}^D$, then there exists a set of natural numbers $\{d_i\}_{i=0}^{D+1} \subset \mathbb{N}$ with $d_0 = m$ and $d_{D+1} = n$, a set affine transformations $\{A_i : \mathbb{R}^{d_i} \rightarrow \mathbb{R}^{d_{i+1}}\}_{i=0}^D$, such that, for $\mathbf{x} \in \mathbb{R}^m$,

$$\begin{cases} h^0(\mathbf{x}) = \mathbf{x}, \\ h^{i+1}(\mathbf{x}) = \alpha(A_i h^i(\mathbf{x})) \text{ for } 0 \leq i < D, \\ \psi(\mathbf{x}) = A_D h^D(\mathbf{x}). \end{cases} \quad (22)$$

Specific universality properties of $\Psi_{m,n}^D(\alpha)$ are proven in [34]. Fix $D, m, n \in \mathbb{N}$, non-constant activation function α , and a continuous function $f : \mathcal{X} \subseteq \mathbb{R}^m \rightarrow \mathbb{R}^n$ over compact set \mathcal{X} . For any $\epsilon > 0$, there exists some $\psi \in \Psi_{m,n}^D$ such that $\rho(f, \psi) < \epsilon$, where:

$$\rho(f, \psi) = \sup_{\mathbf{x} \in \mathbb{R}^m} \|f(\mathbf{x}) - \psi(\mathbf{x})\|_1, \quad (23)$$

and $\|\cdot\|_1$ is the ℓ^1 -norm. That is, for any $\mathbf{x} = (x_1, x_2, \dots, x_m)^T \in \mathbb{R}^m$, $\|\mathbf{x}\|_1 = \sum_{i=1}^m |x_i|$.

This strong result guarantees the existence of some element in the class of neural networks that is arbitrarily close to any continuous function. For this reason, we say that $\Psi_{m,n}^D(\alpha)$ is dense in the space of continuous functions. The following lemma is an immediate consequence of this result.

Lemma 1. *For any $n, m \in \mathbb{N}$, any continuous function $f : \mathcal{X} \subseteq \mathbb{R}^m \rightarrow \mathbb{R}^n$, any non-constant activation function α , and for all $\epsilon > 0$, there exists some $d \in \mathbb{N}$, an affine transformations, $A : \mathbb{R}^m \rightarrow \mathbb{R}^d$, and a matrix $B \in \mathbb{R}^{d \times n}$, such that $\rho(f, B(\alpha \circ A)) < \epsilon$.*

This lemma is useful for proving an important result about a particular subclass of the neural networks we denote as $\Phi_{m,n}^D(\alpha)$.

If a function $\phi \in \Phi_{m,n}^D(\alpha)$, there exists a set of natural numbers $\{d_i\}_{i=0}^{D+1} \subset \mathbb{N}$ with $d_0 = m$ and $d_{D+1} = n$, a set of affine transformations $\{A_i : \mathbb{R}^{d_i} \rightarrow \mathbb{R}^{d_{i+1}}\}_{i=0}^{D-1}$, a set of matrices $\{W_i \in \mathbb{R}^{d_i \times n}\}_{i=0}^D$, such that, for $\mathbf{x} \in \mathbb{R}^m$,

$$\begin{cases} h^1(\mathbf{x}) = \alpha(A_0 \mathbf{x}), \\ h^{i+1}(\mathbf{x}) = \alpha(A_i h^i(\mathbf{x})) \text{ for } 0 \leq i < D, \\ \phi(\mathbf{x}) = W_0 \mathbf{x} + \sum_{i=1}^D W_i h^i(\mathbf{x}). \end{cases} \quad (24)$$

Let $\Phi_{m,n}^D(\alpha)$ be the function class in which to search for an optimal kinematic reconstruction method.

To guarantee the existence of a function in this class that can approximate any continuous function to arbitrary accuracy, we now prove theorem 1, providing similar universality properties as previously mentioned. Moreover, the theorem also shows that the error necessarily decreases as the depth of the network increases, or, in other words, as the number of terms in the summation in equation 24 increases.

Theorem 1. *With fixed non-zero natural numbers D , m , and n , continuous function $f : \mathcal{X} \subseteq \mathbb{R}^m \rightarrow \mathbb{R}^n$, for any $\epsilon > 0$, there exists some $\phi \in \Phi_{m,n}^D(\alpha)$ such that $\rho(f, \phi) < \epsilon$.*

Moreover, if $\phi(\mathbf{x}) = W_0\mathbf{x} + \sum_{i=1}^D W_i h^i(\mathbf{x})$, as defined as in equation 24, and for natural number $1 \leq k \leq D$, define $\epsilon_k = \rho(f, W_0 + \sum_{i=1}^k W_i h^i(\cdot))$, then the optimal, nontrivial, parameters defining ϕ can be selected such that $\epsilon_{k+1} < \epsilon_k$.

Proof. We prove the result inductively on the depth D .

Choose some activation function α . For any matrix $W_0 \in \mathbb{R}^{m \times n}$, define the continuous function $e_0(\mathbf{x}) := f(\mathbf{x}) - W_0\mathbf{x}$ for $\mathbf{x} \in \mathbb{R}^m$. The function $e_0 : \mathcal{X} \subseteq \mathbb{R}^m \rightarrow \mathbb{R}^n$ is a residual between the target function f and an initial linear approximation by W_0 .

By lemma 1, for any $\epsilon > 0$ there exists some affine transformation $A_0 : \mathbb{R}^m \rightarrow \mathbb{R}^{d_1}$ and matrix $W_1 \in \mathbb{R}^{d_1 \times n}$ such that $\rho(f - W_0, W_1(\alpha A_0)) < \epsilon$. Therefore, $\rho(f, W_0 + W_1(\alpha A_0)) < \epsilon$ and $\Phi_{m,n}^1(\alpha)$ is dense in the space of continuous functions.

Call $h^1(\mathbf{x}) = \alpha(A_0\mathbf{x})$ the hidden layer of the network.

Define $\epsilon_1 := \rho(f, W_0\mathbf{x} + W_1 h^1(\mathbf{x}))$.

Note that by its continuity, h^1 is a function mapping \mathcal{X} onto a compact subset of \mathbb{R}^{d_1} . Call this compact subset H .

Continue to define another continuous, residual function, $e_1 : \mathcal{X} \subseteq \mathbb{R}^m \rightarrow \mathbb{R}^n$,

$$e_1(\mathbf{x}) = f(\mathbf{x}) - W_0\mathbf{x} - W_1 h^1(\mathbf{x}). \quad (25)$$

Construct a function γ such that for all $\mathbf{x} \in \mathcal{X}$, $\gamma(h^1(\mathbf{x})) = e_1(\mathbf{x})$. By this construction, $\gamma|_H$ is continuous. So, by the Tietze Extension Theorem, γ can be continuously extended to a function defined on all of \mathbb{R}^{d_1} .

Again, by lemma 1, there exists some affine transformation $A_1 : \mathbb{R}^{d_1} \rightarrow \mathbb{R}^{d_2}$ and matrix $W_2 \in \mathbb{R}^{d_2 \times n}$ such that $\rho(\gamma, W_2(\alpha A_1)) < \epsilon$. Moreover,

$$\rho(f - W_0 - W_1 h^1(\cdot), W_2 \alpha(A_1(h^1(\cdot)))) < \epsilon \quad (26)$$

and equivalently,

$$\rho(f, W_0 + W_1 h^1(\cdot) + W_2 \alpha(A_1(h^1(\cdot)))) < \epsilon. \quad (27)$$

Therefore, $\Phi_{m,n}^2(\alpha)$ is dense in the space of continuous functions.

Moreover, select A_1 and W_2 such that:

$$(A_1, W_2) = \arg \min_{(A,W)} \rho(f, W_0 + W_1 h^1(\cdot) + W \alpha(A(h^1(\cdot)))) , \quad (28)$$

And define $\epsilon_2 := \rho(f, W_0x + W_1h^1(x) + W_2h^2(x))$, where $h^2(x) = \alpha(A_1h^1(x))$.

Then, excluding any trivial solution to equation 28, then

$$\epsilon_2 < \epsilon_1. \quad (29)$$

A trivial solution would be selecting A_1 and W_2 to be zero.

Assume that $\Phi_{m,n}^I(\alpha)$ is dense in the space of continuous functions. In other words, there exists matrices $\{W_i\}_{i=1}^I$ and affine transformations $\{A_i\}_{i=1}^{I-1}$ such that:

$$\rho\left(f, W_0 + \sum_{i=1}^I W_i h^i(\cdot)\right) < \epsilon \quad (30)$$

with $h^i(\cdot) = \alpha(A_{i-1}h^{i-1}(\cdot))$ for $1 \leq i \leq I$ and h^0 is the identity function.

Define $\epsilon_k := \rho\left(f, W_0 + \sum_{i=1}^k W_i h^i(\cdot)\right)$.

h^I is the final hidden layer of the network. By the continuity of h^I , it is a function mapping \mathcal{X} onto a compact subset of \mathbb{R}^{d_I} . Call this compact subset \mathcal{H} .

Define another continuous, residual function, $e_I : \mathcal{X} \subseteq \mathbb{R}^m \rightarrow \mathbb{R}^n$,

$$e_I(x) = f(x) - \left(W_0 + \sum_{i=1}^I W_i h^i(\cdot)\right)x. \quad (31)$$

Construct a function Γ such that for all $x \in \mathcal{X}$,

$$\Gamma(h^I(x)) = e_I(x). \quad (32)$$

By this construction, $\Gamma|_{\mathcal{H}}$ is continuous. So, by the Tietze Extension Theorem, Γ can be continuously extended to a function defined on all of \mathbb{R}^{d_I} .

Again, by lemma 1, there exists some affine transformation $A_I : \mathbb{R}^{d_1} \rightarrow \mathbb{R}^{d_2}$ and matrix $W_{I+1} \in \mathbb{R}^{d_2 \times n}$ such that $\rho(\Gamma, W_{I+1}\alpha A_I) < \epsilon_{I+1}$. Moreover,

$$\rho\left(f - \left(W_0 + \sum_{i=1}^I W_i h^i(\cdot)\right), W_{I+1}\alpha A_I\right) < \epsilon \quad (33)$$

and equivalently,

$$\rho\left(f, W_0 + \sum_{i=1}^{I+1} W_i h^i(\cdot)\right) < \epsilon. \quad (34)$$

Moreover, select A_I and W_{I+1} such that:

$$(A_I, W_{I+1}) = \arg \min_{(A,W)} \rho \left(f, W_0 + \sum_{i=1}^I W_i h^i(\cdot) + W \alpha(A(h^{I+1}(\cdot))) \right). \quad (35)$$

Then, again, excluding any trivial solution to equation 35,

$$\epsilon_{I+1} < \epsilon_I. \quad (36)$$

Thus, $\Phi_{m,n}^{I+1}(\alpha)$ is dense in the space of continuous functions, which inductively shows that for any non-zero natural number D , $\Phi_{m,n}^{I+1}(\alpha)$ is dense in the space of continuous functions, or, more specifically, there exists some $\phi \in \Phi_{m,n}^D(\alpha)$, defined

$$\phi(\mathbf{x}) = W_0 \mathbf{x} + \sum_{i=1}^D W_i h^i(\mathbf{x}) \quad (37)$$

such that

$$\rho(f, \phi) < \epsilon. \quad (38)$$

Therefore, $\Phi_{m,n}^D(\alpha)$ has the desired universality property.

Furthermore, ϕ can be selected in a way in which $\epsilon_{k+1} < \epsilon_k$.

□

3.2 Optimization methods

In any given problem to be solved with the NN, the task is to choose an optimal function from the class $\mathcal{F} = \Phi_{m,n}^D(\alpha)$ to be a functional relationship between a set of input variables \mathbf{x} and a set of response variables \mathbf{y} .

Each function $\phi \in \mathcal{F}$ is completely determined by the elements of the matrices and vectors that determine the values of the hidden layers. Let $\omega \in \mathbb{R}^p$ be the collection of all these elements, where p is the total number of them. We can then write for any $\mathbf{x} \in \mathbb{R}^m$: $\phi(\mathbf{x}) = \phi_\omega(\mathbf{x})$.

Choosing an optimal function from this class entails finding the collection of parameters ω in \mathbb{R}^p that minimizes $\mathcal{L}_{\mathcal{D}}$, the expected discrepancy or generalization error between \mathbf{y} and $\phi_\omega(\mathbf{x})$, over the joint probability distribution of \mathbf{x} and \mathbf{y} , \mathcal{D} , defined by:

$$\mathcal{L}_{\mathcal{D}}(\omega) = \mathbb{E}_{\mathbf{x}, \mathbf{y} \sim \mathcal{D}} \ell(\omega, \mathbf{x}, \mathbf{y}) = \int \ell(\omega, \mathbf{x}, \mathbf{y}) d\mathcal{D}(\mathbf{x}, \mathbf{y}), \quad (39)$$

where ℓ is some loss function measuring the discrepancy between y and $\phi_\omega(\mathbf{x})$.

With a randomly sampled data set $\{\mathbf{x}_i, y_i\}_{i=1}^N$, if N is sufficiently large, then the generalization error can be approximated by an empirical error:

$$\mathcal{L}_{\mathcal{D}} \approx \frac{1}{N} \sum_{i=1}^N \ell(\omega, \mathbf{x}_i, y_i). \quad (40)$$

This summation is sometimes called the fidelity term, as it measures the discrepancy between the data and model predictions. A commonly used fidelity term is the mean square error, with:

$$\ell(\omega, \mathbf{x}_i, y_i) = \|y_i - \phi_\omega(\mathbf{x}_i)\|_2^2. \quad (41)$$

The fidelity term used in this study is a modification of this, the mean square logarithmic error:

$$\ell(\omega, \mathbf{x}_i, y_i) = \|\log(y_i) - \log(\phi_\omega(\mathbf{x}_i))\|_2^2. \quad (42)$$

Due to the universality of neural networks, there is a model that can achieve zero empirical error. However, in the presence of noise this means the model can overfit to the data sample and lose its generalizability. This problem can be addressed by adding a regularization term to the optimization problem as a penalty for certain irregular behavior. Common regularization terms include the ℓ^2 -norm, used to limit the size of the parameters, and the ℓ^1 -norm, which can induce sparse solutions. For our analysis we choose the ℓ^1 -regularization. The Theorem 1.3 in [35] and Proposition 27 of [36] provide an evidence that minimizing the ℓ^1 norm provides sparse optimal solutions with a minimal number of nonzero elements. Well-constructed models should be able to generalize the information from one given sample to any possible event. Thus, regularization with the ℓ^1 norm produces a model determined by a minimal number of parameters so that the optimal solution does not fit completely to the training set and lose its generalizability.

Therefore, the determination of an the optimal neural network model consists of minimizing this final loss function, the sum of the sample fidelity term and with a weighted regularization term:

$$\min_{\omega \in \mathbb{R}^p} \frac{1}{N} \sum_{i=1}^N \ell(\omega, \mathbf{x}_i, y_i) + \lambda \cdot \|\omega\|_1, \quad (43)$$

where ℓ is defined in Eq. 42 and λ is a hyperparameter to determine the magnitude of the regularization.

Expression 43 can be minimized using stochastic gradient methods on batches of the data sample [37]. The training is accelerated using classical momentum methods [38].

In particular, by randomly selecting ω^0 , appropriately selecting a sequence of step sizes, or learning rates, η^k that diminishes to zero, randomly selecting a batch $I \subset \{1, \dots, N\}$, choosing a momentum parameter μ , and by defining:

$$v^{k+1} = \mu v^k - \eta^k \nabla_{\omega} L_I(\omega^k), \quad (44)$$

$$\omega^{k+1} = \omega^k + v^{k+1}. \quad (45)$$

Then the sequence ω^k converges to a set of parameters defining the optimal neural network with the minimal generalization error, in the sense described here.

3.3 The model

We construct a model to rigorously weight classically derived reconstructions of x and Q^2 with corrections based on measurements from the final state lepton and hadronic system. The final reconstruction of these observables with the neural network approach are labeled below as Q_{NN}^2 and x_{NN} respectively.

The constructed model is an ensemble of networks from the previously defined function class $\Phi_{m,1}^D(\alpha)$, where α is the rectified linear unit (ReLU). The values of D and m vary with each network in the ensemble.

The NC DIS events studied in this analysis are by definition the events containing the scattered electron in the final state, therefore we aim to reconstruct the Q_{NN}^2 primarily from the related observables, i.e. using the properties of electron directly measured in the experiment. In particular, as we use as inputs three set of variables: the classically reconstructed kinematic observables ($Q_{EL}^2, Q_{DA}^2, Q_{JB}^2$), measurements on the scattered lepton (E_{ν}, θ_{ν}), and measurements on the final-state hadronic system ($\delta_{\mathcal{H}}, P_{T,\mathcal{H}}$). We reconstruct the Q^2 in the form:

$$Q_{NN}^2 = A_{Q^2}(Q_{EL}^2, Q_{DA}^2, Q_{JB}^2) + L_{Q^2}(A_{Q^2}, E_{\nu}, \theta_{\nu}) + H_{Q^2}(A_{Q^2}, \delta_{\mathcal{H}}, P_{T,\mathcal{H}}), \quad (46)$$

in which A_{Q^2} could be understood as a rigorous average of classically derived reconstructions, L_{Q^2} is a correction term computed from the scattered lepton, and H_{Q^2} is another correction term computed from the final-state hadronic system. In our analysis $A_{Q^2}, L_{Q^2}, H_{Q^2}$ are networks in $\Phi_{3,1}^5(\alpha)$, with each hidden layer of the networks containing 2000 nodes.

The x observable for the NC DIS events is actually calculated from the electron-related observables as well. Therefore, we reconstruct x_{NN} , with Q_{NN}^2 also as an input, for a

total of eight inputs $(x_{EL}, x_{DA}, x_{JB}, E_{l'}, \theta_{l'}, \delta_{\mathcal{H}}, P_{T,\mathcal{H}}, Q_{NN}^2)$, in the form:

$$x_{NN} = A_x(x_{EL}, x_{DA}, x_{JB}) + L_x(A_x, Q_{NN}^2, E_{l'}, \theta_{l'}) + H_x(A_x, Q_{NN}^2, \delta_{\mathcal{H}}, P_{T,\mathcal{H}}), \quad (47)$$

where A_x , L_x , and H_x are defined similarly to A_{Q^2} , L_{Q^2} , and H_{Q^2} , but A_x is a network in $\Phi_{3,1}^{20}(\alpha)$ with each hidden layer containing 1000 nodes, and L_x , H_x are networks in $\Phi_{4,1}^{10}(\alpha)$, with each hidden layer containing 500 nodes.

In the ensemble neural network model, we used as the nonlinear activation function the ReLU :

$$\alpha(x) = \max(x, 0). \quad (48)$$

It has been shown that with a gradient descent algorithm [39], using the ReLU function as the activation function provides a smaller training time compared to that with the use of functions with saturating nonlinearities, such as a sigmoid or hyperbolic tangent function. The reduced training time enabled us to experiment with more sophisticated networks. In addition to this, the ReLU functions do not need input normalization to prevent them from saturating, which is a desirable property for the present analysis.

To accommodate for the large range of the Q^2 and x variables in the analysis, we select the loss function defined in Eq. 42 for the training of the DNN models.

4 Experimental setup

The Monte Carlo simulated events used to train our deep neural networks were specifically generated using the conditions of $e^\pm p$ scattering in the ZEUS detector at HERA. A detailed description of the ZEUS detector can be found elsewhere [8].

In our analysis we have used two samples of Monte Carlo simulated e^+p DIS events that are provided by the ZEUS collaboration. These samples were generated using the ARIADNE and LEPTO MCEGs with the matrix elements for the DIS process calculated in the HERACLES [12] package. For both samples the same set of kinematic cuts was applied during the generation, the same PDFs CTEQ5D [40] were assumed and the same hadronization settings were used to model the hadronization with the Pythia6 program. Therefore, the essential difference between the two samples is the way the higher order corrections are partially modeled with the corresponding algorithms (QCD cascades). Namely, the LEPTO MCEG utilized the parton shower approach [41], while ARIADNE implements a color-dipole model [42].

The generated particle-level events were passed through the ZEUS detector and trigger simulation programs based on Geant 3.21 [26] assuming the data taking and trigger conditions of the ZEUS experiment in the year 2007. The simulated detector response was

processed and reconstructed using exactly the same software chain and the same procedures as being used for real data. The results of the processing were saved in ROOT [43] files in a form of ZEUS Common NTuples [30, 31], a format that can be easily used for physics analysis without any ZEUS-specific software.

5 Event selection

The selection of events for the neural network training is motivated by the selection procedure applied in the previous ZEUS analyses of hadronic final state in DIS [44–49]. Even though the presented analysis performed on the Monte Carlo simulated events, the cuts are selected and applied as if the analysis is performed on real data for the purpose of being as close as possible the measurements. The general motivation for these cuts is the same as in many analyses performed by the ZEUS collaboration: to define unambiguously the phase space of the measurement, ensure low fraction of background events, and a reasonable description of detector acceptance by Monte Carlo simulations.

5.1 Phase space selection

The phase space for the training of the neural networks in this analysis is selected as $100 \text{ GeV}^2 < Q^2 < 20480 \text{ GeV}^2$, being close to the phase space of physics analysis in Ref. [48].

In the phase-space region at low x and very low inelasticity y , the QED predictions from the Monte Carlo simulations are not reliable because of a limit of higher orders in the calculations [50]. To avoid these phase-space regions, the events are required to have $y_{JB} \cdot (1 - x_{DA})^2 > 0.004$. To ensure sufficient reliability of Monte Carlo simulations, it is required that $y_{JB} > 0.04$ [50]. To ensure the optimal electron identification and electron energy resolution, similarity to the previous physics analyses a kinematic cut $0.2 < y_{EL} < 0.7$ is used.

5.2 Event selection

The deep inelastic scattering events of interest are those characterized by the presence of a scattered electron in the final state and a significant deposit of energy in the calorimeter from the hadronic final state. The scattered electrons are registered in the detector as localized energy depositions primarily in the electromagnetic part of the calorimeter, with little energy flow into the hadronic part of the calorimeter. On the other hand, hadronic showers travel much more extensively, both transversely and longitudinally.

In addition to the DIS process, there are also background processes which leave in detector signatures similar to those described above. Therefore, the correct and efficient identification of the scattered lepton is crucial for the selection of the NC DIS events. For this analysis, the **SINISTRA** algorithm is used to identify lepton candidates [9]. Based on the information from the detector and the results of the **SINISTRA** algorithm, the following selection criteria are applied to select the events for the further analysis:

- **Detector status:** It is required that for all the events the detector was functional.
- **Electron energy:** At least one electron candidate with energy greater than 10 GeV [48] is identified in the event.
- **Electron identification probability:** The **SINISTRA** [9] probability of lepton candidate being the DIS lepton was required to be greater than 90%. If several lepton candidates satisfied this condition, the candidate with the highest probability is used. In addition to this, there must be no problems reported by the **SINISTRA** algorithm.
- **Electron isolation:** To assist in removing events where the energy deposits from the hadron system overlap with those of the scattered lepton, the fraction of the energy not associated to the lepton is required to be less than 10% over the total energy deposited within a cone around the lepton candidate. The cone is defined with a radius of 0.7 units in the pseudorapidity-azimuth plane around the lepton momentum direction [48].
- **Electron track matching:** The tracking system covers the region of polar angles restricted to $0.3 < \theta < 2.85$ rad. Electromagnetic clusters within that region that have no matching track are most likely photons. If the lepton candidate is within the tracking system acceptance region, there must be a matched track. This track must have a distance of closest approach between the track extrapolation point at the front surface of the CAL and the cluster center-of-gravity-position of less than 10 cm. The track energy must be greater than 3 GeV [48].
- **Electron position:** To minimize the impact of imperfect simulation of some detector regions, additional requirements on the position of the electromagnetic shower are imposed. The events in which the lepton was found in the following regions are rejected [51]:
 - $\sqrt{x^2 + y^2} < 18$ cm, regions close the the beam pipe
 - $z < -148$ cm and $y > 90$ cm and $-14 < x < 12$ cm, a part of the RCAL where the depth was reduced due to the cooling pipe for the solenoid (chimney),
 - $-104 < z < -98.5$ cm or $164 < z < 174$ cm, regions in-between calorimeter sections (super-crack).

- **Primary vertex position:** It was required that the reconstructed primary vertex position is close to the central region of the detector, implying $-28.5 < Z_{\text{vtx}} < 26.7$ cm [48].
- **Energy-longitudinal momentum balance:** To suppress photoproduction and beam-gas interaction background events and imperfect Monte Carlo simulations of those, restrictions are put on the energy-longitudinal momentum balance. This quantity is defined as:

$$\delta = \delta_l + \delta_{\mathcal{H}} = (E_{l'} - P_{z,l'}) + (E_{\mathcal{H}} - P_{z,\mathcal{H}}) = \sum_i (E_i - P_{z,i}), \quad (49)$$

where the final summation index runs over all energy deposits in the detector. In this analysis, we apply a condition of $38 < \delta < 65$ GeV [48].

- **Missing transverse energy:** To remove the beam-related background and the cosmic-ray events a cut on the missing energy is imposed. $P_{T,\text{miss}}/\sqrt{E_T} < 2.5$ GeV^{1/2}, where E_T is the total transverse energy in the CAL and $P_{T,\text{miss}}$ is the missing transverse momentum – the transverse component of the vector sum of the hadronic final state and scattered electron momenta.

6 Training the neural network models

We use the neural network models defined in Sec. 3.3 and consider them as optimization problem in terms of Eq. 43, i.e., we minimize the loss function across the selected training set and satisfy sparse regularity conditions. The optimal regularity condition depends on the selection of the training set, the events batch size, the initial learning rate, and the regularization parameter. We aim to select these in a way that minimizes overfitting in particular regions of the kinematic space while still maximizing the mean accuracy of the model.

We select a set of events for training as described in Sec. 5 and define the true values of the Q^2 and x observables as described in Sec. 2.3. Fig. 3 shows a distribution of selected events on the $(x_{\text{true}}, Q_{\text{true}}^2)$ plane and the boundaries of the analysis bins.

Next, we fix the regularization parameter \mathcal{R} to 10^{-5} and select optimal parameters for the learning rate \mathcal{L} and batch size \mathcal{B} experimentally by varying the learning rate against the batch size. The appropriate selection of these parameters ensures fast convergence of the stochastic gradient method by balancing noise in the gradients with the stability of the algorithm. For each set of parameters, ten attempts are made and the best result in terms of the mean square error of the x reconstruction model over the training set

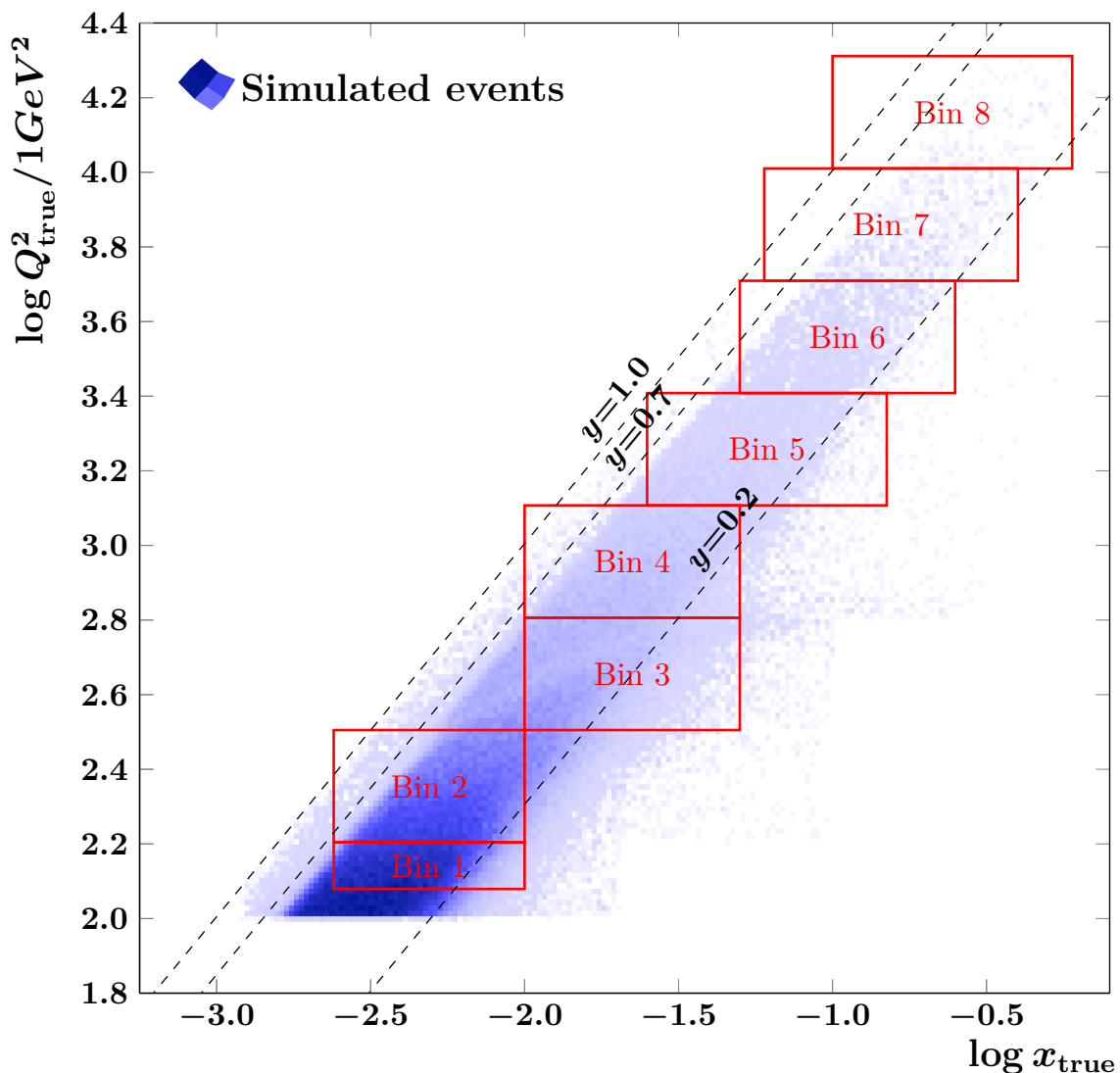


Figure 3: *Distribution of events from the training set in $(x_{\text{true}}, Q_{\text{true}}^2)$ plane and the boundaries of the analysis bins from Tab. 3.*

is chosen. The results are listed in Tab. 1. The smaller learning rate assures a higher stability of the results than a larger learning rate. It prolongs the training process but avoids a poor convergence of the learning process as observed for larger learning rates. The larger batch size does not offer any advantages in our analysis as shown in Tab. 1. We, therefore, select an initial learning rate of 10^{-5} with a minimal batch size. To choose the regularization parameter close to the optimal one, we vary its value with constant batch size of 10000 and initial learning rate of 10^{-5} and again observe the mean square error of the x reconstruction model over the training set. For each set of parameters, ten attempts are made and the best result is chosen. The results are presented in Tab. 2. Accordingly, we choose a regularization parameter of 10^{-6} . Following the suggestions in

| | RMS of $\log x - \log x_{\text{true}}$ | | |
|----------------------|--|---------------|---------------|
| \mathcal{L} | \mathcal{B} | \mathcal{B} | \mathcal{B} |
| | 10000 | 50000 | 100000 |
| 1.0×10^{-7} | 0.1507 | 0.1523 | 0.1598 |
| 5.0×10^{-7} | 0.1568 | 0.1575 | 0.1575 |
| 1.0×10^{-6} | 0.1504 | 0.1585 | 0.1547 |
| 5.0×10^{-6} | 0.2384 | 0.2284 | 0.1829 |
| 1.0×10^{-5} | 0.2182 | 2.5972 | 2.2767 |
| 1.5×10^{-5} | 0.2122 | 1.7751 | 1.6028 |
| 2.0×10^{-5} | 3.0258 | 0.2607 | 0.2852 |
| 5.0×10^{-5} | 3.6962 | 2.4858 | 3.1231 |

Table 1: Resolution of $\log x$ reconstruction after 200 epochs of training with different values of initial learning rate \mathcal{L} and batch size \mathcal{B} .

| \mathcal{R} | RMS of $\log x - \log x_{\text{true}}$ |
|----------------------|--|
| 1.0×10^{-6} | 0.1493 |
| 1.0×10^{-5} | 0.1494 |
| 1.0×10^{-4} | 0.1484 |

Table 2: Resolution of $\log x$ reconstruction after 200 epochs of training with different values of regularization parameter \mathcal{R} .

Ref. [52], we start with a small batch size, and increase it in initial training epochs. We test this approach by comparing the mean square error of the x reconstruction model over the training set over the first 200 epochs of training over three different training regimes. The results are summarized in Fig. 4 and imply to use a gradually increasing batch size up to a maximum batch size of 1000.

7 Results

The performance of our DNN-based reconstruction of DIS kinematics is compared to the performance of the electron method, the Jacques-Blondel method, and the double-angle methods using data-sets independent from those used for the training. The main quantities of the comparison are the resolutions of the reconstructed variables $\log Q^2/1 \text{ GeV}^2$ and $\log x$ as measured in selected $x - Q^2$ regions (bins). The resolutions are defined as RMS of the distributions $\log Q^2/1 \text{ GeV}^2 - \log Q_{\text{true}}^2/1 \text{ GeV}^2$ and $\log x - \log x_{\text{true}}$. The boundaries of the bins are given in Tab. 3 and are chosen to be close to the bins used in ZEUS DIS analyses, e.g., in Ref. [46].

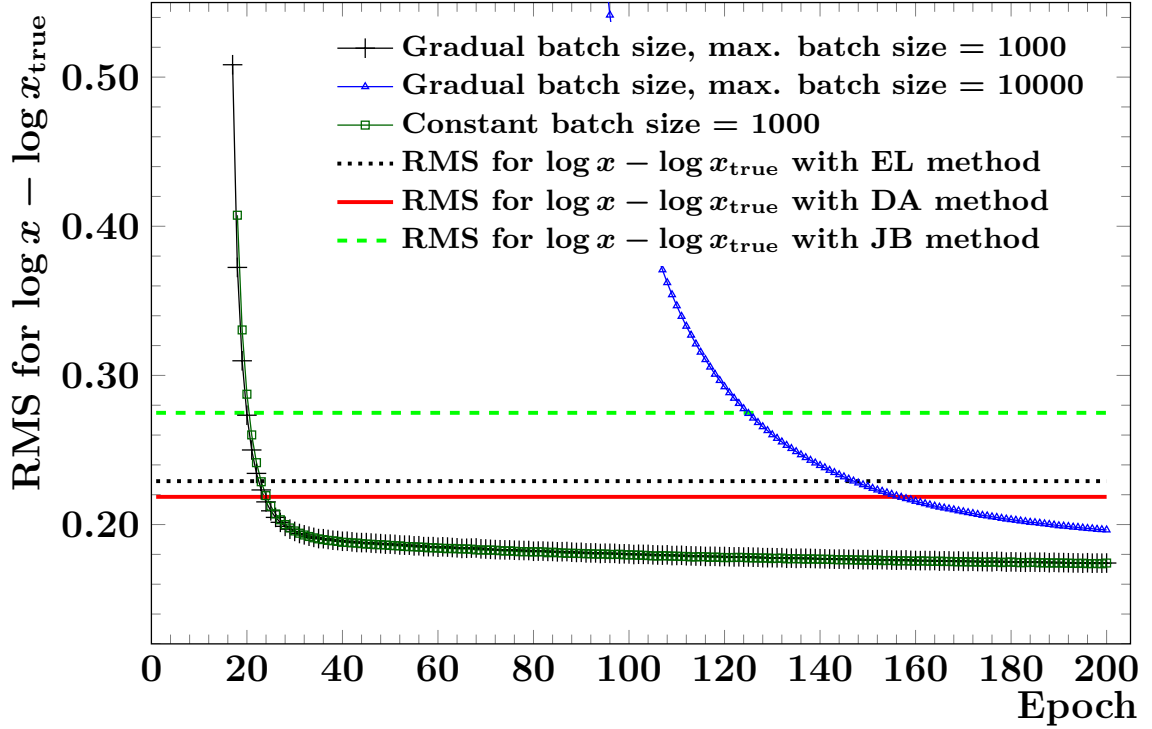


Figure 4: Training history for x reconstruction model using different training parameters but the same Q^2 reconstruction model obtained with $\mathcal{L} = 1.0 \times 10^{-5}$, $\mathcal{R} = 1.0 \times 10^{-6}$ and $\mathcal{B} = 10000$. For all the cases of the x reconstruction model training the initial learning rate was set to $\mathcal{L} = 1.0 \times 10^{-5}$ and the regularization parameter to $\mathcal{R} = 1.0 \times 10^{-6}$.

| Bin | Q^2 (GeV 2) | x |
|-----|-------------------|----------------|
| 1 | 120 - 160 | 0.0024 - 0.010 |
| 2 | 160 - 320 | 0.0024 - 0.010 |
| 3 | 320 - 640 | 0.01 - 0.05 |
| 4 | 640 - 1280 | 0.01 - 0.05 |
| 5 | 1280 - 2560 | 0.025 - 0.150 |
| 6 | 2560 - 5120 | 0.05 - 0.25 |
| 7 | 5120 - 10240 | 0.06 - 0.40 |
| 8 | 10240 - 20480 | 0.10 - 0.60 |

Table 3: Kinematic bins in x and Q^2 , see also Fig. 3.

The distributions of the $\log Q^2/1 \text{ GeV}^2 - \log Q_{\text{true}}^2/1 \text{ GeV}^2$ and $\log x - \log x_{\text{true}}$ quantities are given in the Fig. 5 and Fig. 6, respectively. The numerical values for the resolutions are summarized for all the bins and methods in Tab. 4. In addition to that, Fig. 7 and Fig. 8 show the two dimensional distributions of events in $\log Q^2/1 \text{ GeV}^2$ vs. $\log Q_{\text{true}}^2/1 \text{ GeV}^2$ and $\log x$ vs. $\log x_{\text{true}}$ planes.

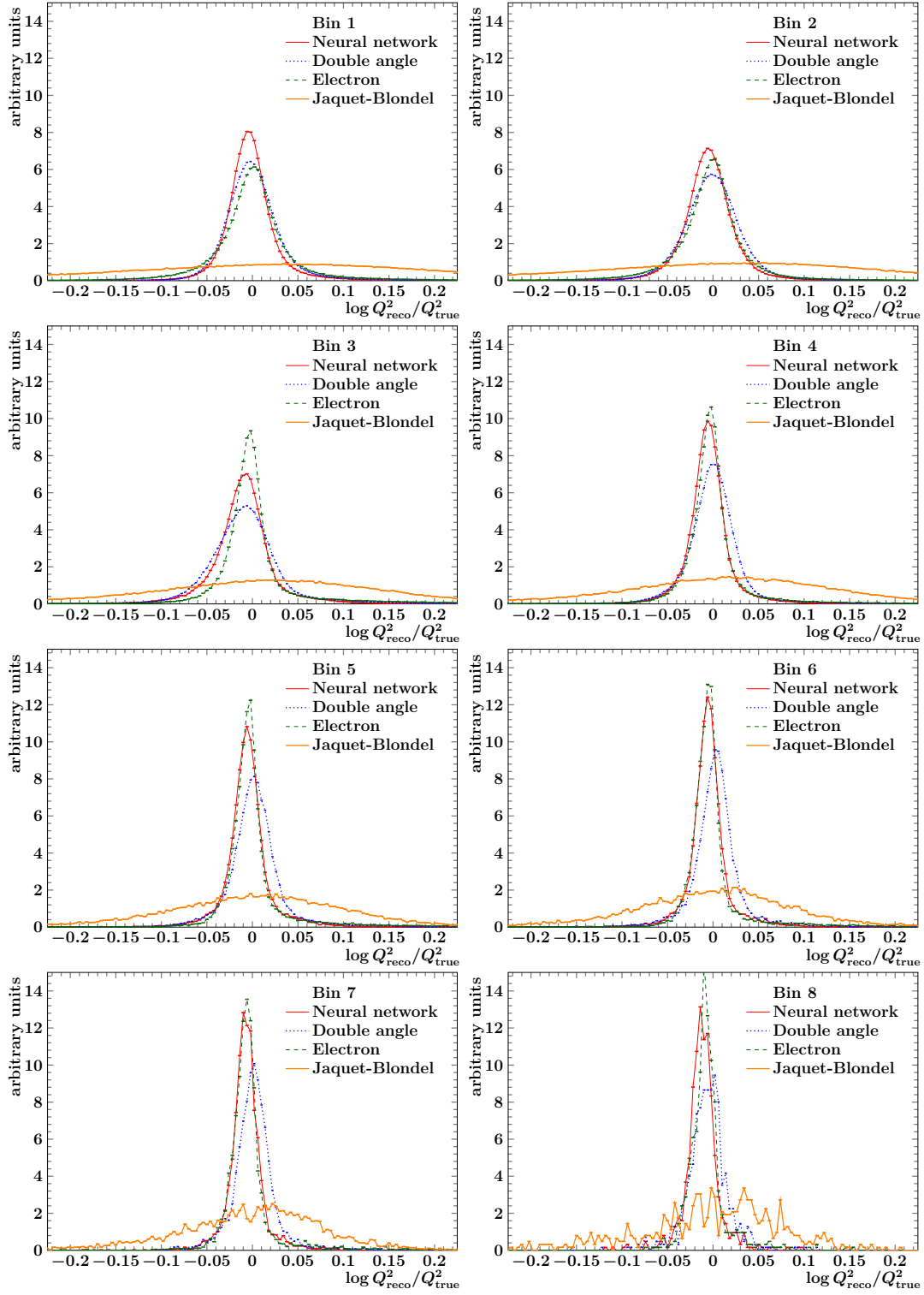


Figure 5: Distributions of $\log Q^2/1 \text{ GeV}^2 - \log Q^2_{\text{true}}/1 \text{ GeV}^2$ for different reconstruction methods in individual analysis bins. For a better visibility, the centers of bins in each distribution connected with straight lines.

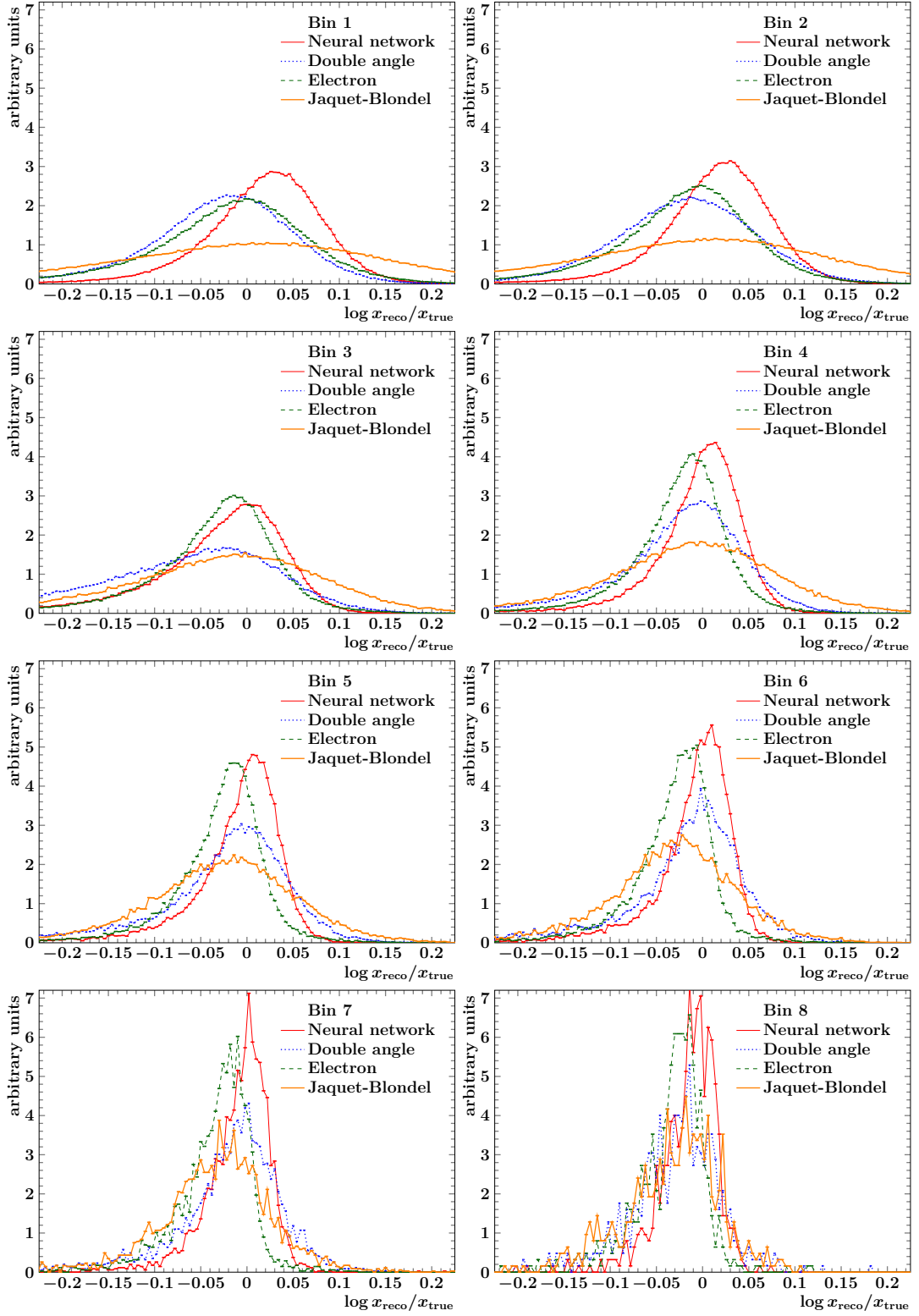


Figure 6: Distributions of $\log x - \log x_{\text{true}}$ for different reconstruction methods in individual analysis bins. For a better visibility, the centers of bins in each distribution connected with straight lines.

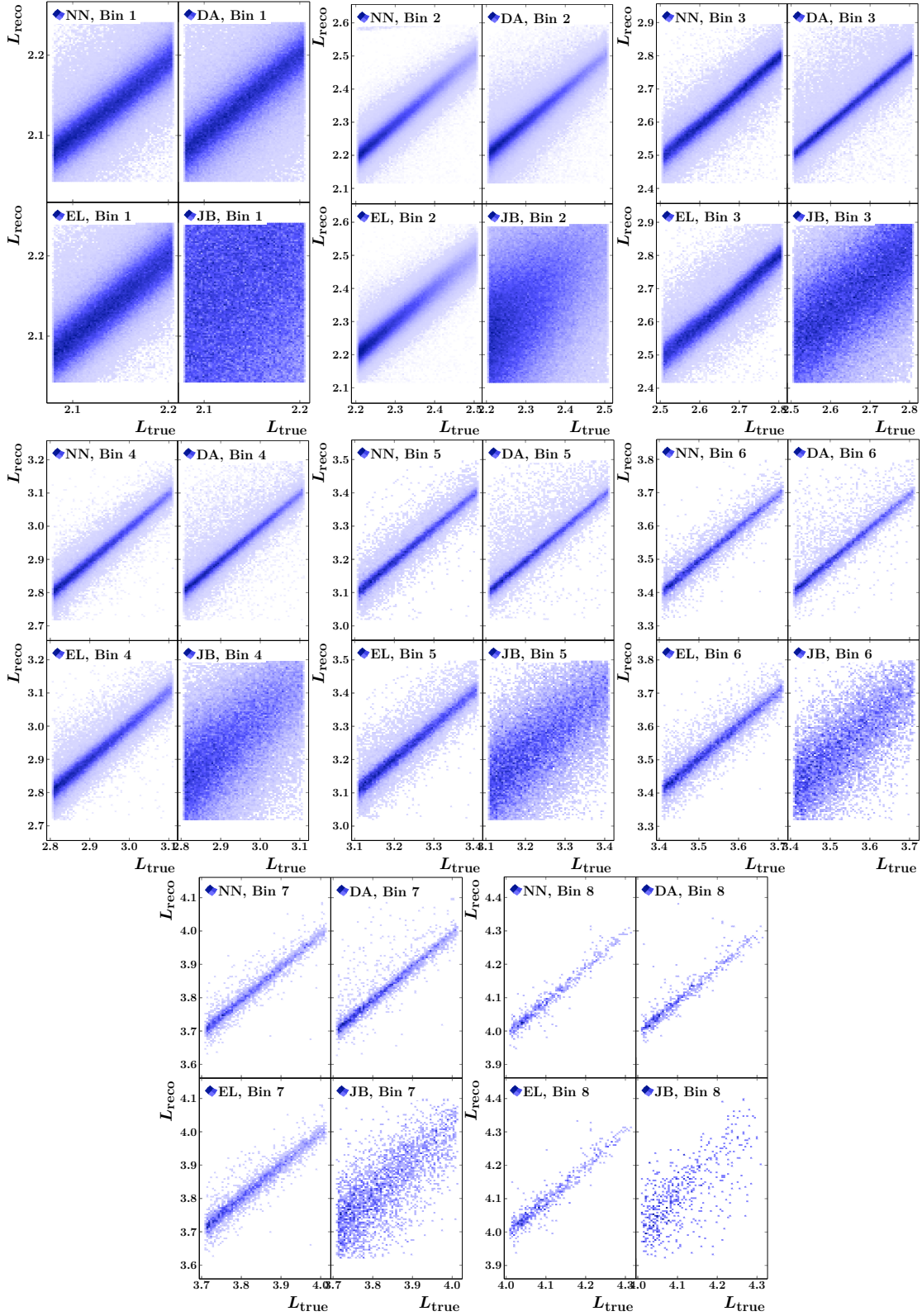


Figure 7: Distribution of events in $L_{\text{reco}} = \log Q^2/1 \text{ GeV}^2$ versus $L_{\text{true}} = \log Q^2_{\text{true}}/1 \text{ GeV}^2$ plane for different reconstruction methods in individual analysis bins.

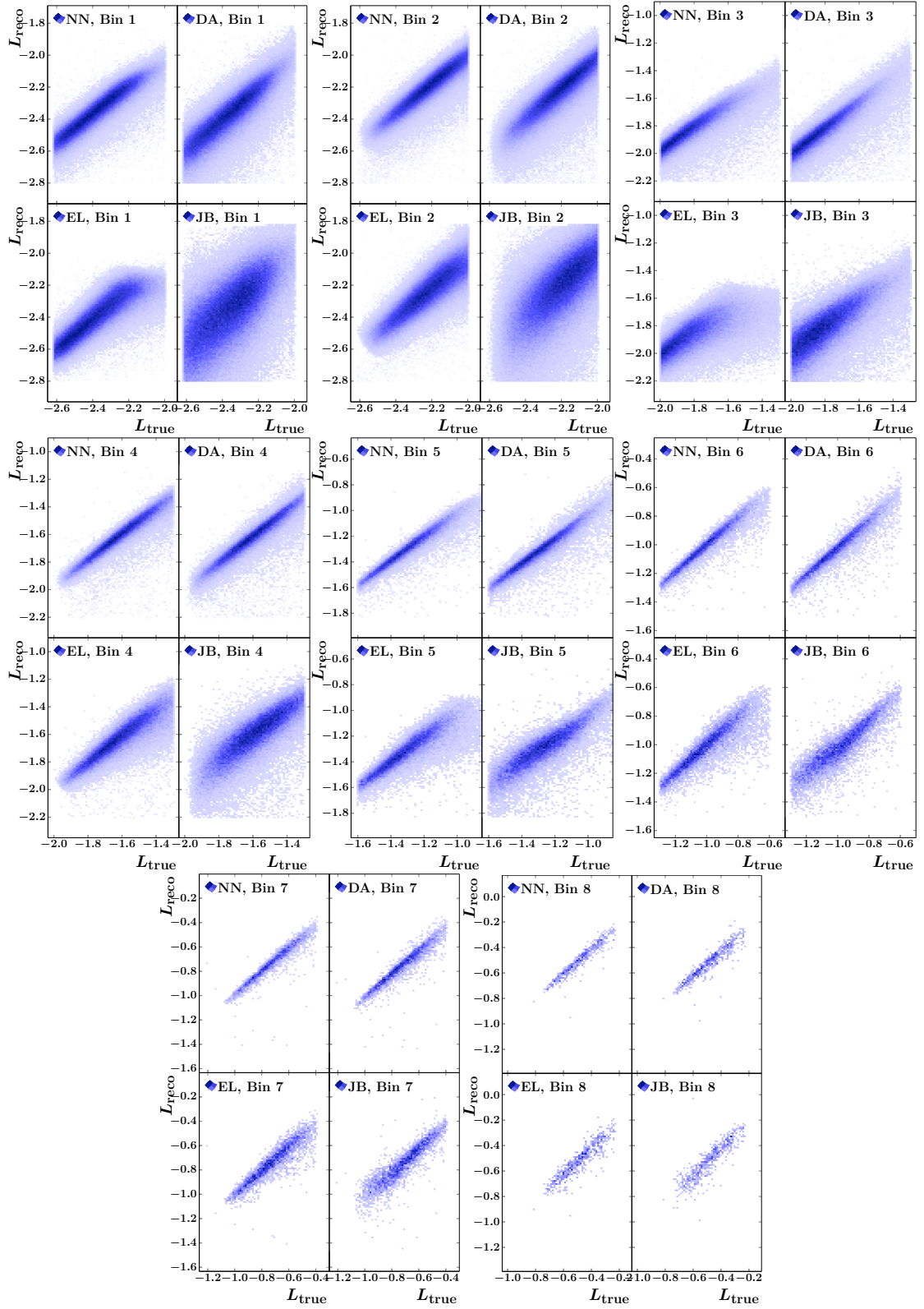


Figure 8: *Distribution of events in $L_{\text{reco}} = \log x$ versus $L_{\text{true}} = \log x_{\text{true}}$ plane for different reconstruction methods in individual analysis bins.*

| Bin | Events | Resolution of $\log x$ | | Resolution of $\log Q^2/1 \text{ GeV}^2$ | |
|-----|--------|------------------------|----------------------------------|--|---|
| 1 | 301780 | NN: 0.070 | EL: 0.083 JB: 0.180 DA: 0.103 | NN: 0.035 | EL: 0.035 JB: 0.203 DA: 0.062 |
| 2 | 350530 | NN: 0.069 | EL: 0.082 JB: 0.167 DA: 0.096 | NN: 0.040 | EL: 0.043 JB: 0.192 DA: 0.064 |
| 3 | 138456 | NN: 0.098 | EL: 0.130 JB: 0.138 DA: 0.100 | NN: 0.055 | EL: 0.053 JB: 0.150 DA: 0.077 |
| 4 | 74844 | NN: 0.067 | EL: 0.084 JB: 0.117 DA: 0.077 | NN: 0.044 | EL: 0.046 JB: 0.138 DA: 0.063 |
| 5 | 31043 | NN: 0.064 | EL: 0.091 JB: 0.102 DA: 0.073 | NN: 0.036 | EL: 0.041 JB: 0.117 DA: 0.053 |
| 6 | 11475 | NN: 0.053 | EL: 0.079 JB: 0.083 DA: 0.061 | NN: 0.033 | EL: 0.036 JB: 0.100 DA: 0.045 |
| 7 | 3454 | NN: 0.050 | EL: 0.069 JB: 0.074 DA: 0.055 | NN: 0.036 | EL: 0.038 JB: 0.093 DA: 0.042 |
| 8 | 624 | NN: 0.036 | EL: 0.055 JB: 0.067 DA: 0.045 | NN: 0.033 | EL: 0.037 JB: 0.095 DA: 0.041 |

Table 4: Resolution of the reconstructed kinematic variables in bins of x and Q^2 . The resolution for x and Q^2 is defined as the RMS of the distributions $\log(x) - \log(x_{\text{true}})$ and $\log(Q^2) - \log(Q^2_{\text{true}})$ respectively.

The comparison of our approach with the classical methods is shown in Figs. 5,6,7,8 and summarized in Tab. 4. It demonstrates that the DNN-based approach is well suited for the reconstruction of DIS kinematics. Specifically, for most of the bins, our approach provides the best resolution as measured by the standard deviation of the logarithmic differences. The better performance of the DNN-based approach in most of the bins is a consequence of using additional available information about the final state. In this respect, the DNN-based approach is similar to averaging of the values provided by the classical methods with some weights or to alternative approaches for the same task [53]. However, in addition to a better resolution, the reconstruction with the DNN has two important advantages over the classical methods or any simple combination of them. First, it enables an extension of the model with various physics observables in the most robust way. And second, it allows the use of the desired definition of the kinematic observables, avoiding the intrinsic biases of the other methods.

The resolution of the DNN-based approach is improved in two ways. For the first couple of bins, the main improvement is caused by the more precise estimation of the reconstructed observables. This is clearly seen in Figs. 5 and 6. For the bins with higher Q^2 and x

the main improvement is due to the rejection of outliers, which can be seen in Figs. 7 and 8. The bins with higher Q^2 and x also demonstrate another, very specific advantage on the DNN approach. Due to the low number of training events in the high Q^2 and x region, it would not be possible to train a DNN model or combine the Q^2 and x observables with other methods using information from this region only. However, the DNN training process benefits from the higher number of events available elsewhere in the kinematical space and delivers models that perform well even in the bins with highest Q^2 and x .

8 Conclusions

We have presented the use of DNN to reconstruct the kinematic observables Q^2 and x in the study of neutral current DIS events at the ZEUS experiment at HERA. The DNN models are specially designed to be effective in their universal approximation capability, robust in the sense that increasing the depth of the networks will necessarily reduce empirical error, and computationally efficient with a structure that avoids “vanishing” gradients arising in the backpropagation algorithm.

Compared to the classical reconstruction methods, the DNN-based approach enables significant improvements in the resolution of Q^2 and x . At the same time, it is evident that the usage of the DNN approach allows to match easily any definition of Q^2 and x at the true level that is preferred for a given physics analysis.

The large samples of simulated data required for the training of the DNN can be generated rapidly at modern data centers. Also, DNN allow to effectively extract information from large data sets. This suggests that our new approach for the reconstruction of DIS kinematics can serve as a rigorous method to combine and outperform the classical reconstruction methods at ongoing or upcoming DIS experiments. We will extend the approach beyond inclusive DIS measurements and will study next the use of DNN for the reconstruction of event kinematics in semi-inclusive and exclusive DIS measurements.

Acknowledgments

We are grateful to the ZEUS Collaboration for allowing us to use ZEUS Monte Carlo simulated samples in this analysis. We thank R. Aggarwal, C. Fanelli, Y. Furletova, D. Higinbotham, D. Lawrence, A. Vossen, and R. Yoshida for helpful discussions.

The work of M. Diefenthaler was supported by the US Department of Energy, Office of Science, Office of Nuclear Physics contract DE-AC05-06OR23177, under which Jefferson

Science Associates, LLC operates the Thomas Jefferson National Accelerator Facility.

A. Farhat and Y. Xu were supported in part by National Science Foundation under grant DMS-1912958. A. Farhat was also supported by an EIC Center Fellowship at the Thomas Jefferson National Accelerator Facility.

A Software used in the analysis

The `ROOT` package [43] of version 6.22 was used to read the ZEUS data, analyze it and prepare plain text (or ROOT files) with selected information to be used with the ML tools. The selected information from the plain text (or ROOT) files was piped using the `pandas` package [54] into `Keras` [55] interface to `tensorflow` [56] 2.3.0 library to train the ML models. The packages `Eigen` [57], `frugally-deep` [58], `FunctionalPlus` [59], `JSON for Modern C++` [60] were used for execution of the trained models after these were converted into `frugally-deep` model format [58] to be used with C++ application. The dependencies for the `tensorflow` were supplied from the PyPi repository. The training was performed using libraries for computing on GPUs from the `CUDA` [61] framework of version 10.1.

The analysis codes were compiled and executed on the HPC cluster “Cobra” of Max-Planck Computing and Data Facility in Garching, Germany [62]. The operation system used was Linux on x86_64 architecture using `gcc` [63] of version 7.3 and `python` [64] of version 3.6.8.

The figures with the final results were produced with the `PGFPLOTS` [65] package.

References

- [1] B.H. Wiik et al., HERA - A Proposal for a Large Electron Proton Colliding Beam Facility at DESY.
<https://old.inspirehep.net/record/19436/files/Fulltext.pdf>, 1981.
- [2] DUNE Coll., B. Abi et al., Volume I. Introduction to DUNE. JINST **15**, T08008 (2020). [arXiv:2002.0296](https://arxiv.org/abs/2002.0296).
- [3] F. Gautheron et al., COMPASS-II Proposal.
<https://cds.cern.ch/record/1265628/files/SPSC-P-340.pdf>, 2010.
- [4] G.A. Voss and B.H. Wiik, The Electron proton collider HERA. Ann. Rev. Nucl. Part. Sci. **44**, 413 (1994).
- [5] H1 and ZEUS Colls., H. Abramowicz et al., Combination of measurements of inclusive deep inelastic $e^\pm p$ scattering cross sections and QCD analysis of HERA data. Eur. Phys. J. **C75**, 580 (2015). [arXiv:1506.0604](https://arxiv.org/abs/1506.0604).
- [6] U. Bassler and G. Bernardi, On the kinematic reconstruction of deep inelastic scattering at HERA: The Sigma method. Nucl. Instrum. Meth. **A361**, 197 (1995). [arXiv:hep-ex/9412004](https://arxiv.org/abs/hep-ex/9412004).
- [7] R. Abdul Khaleket et al., Science Requirements and Detector Concepts for the Electron-Ion Collider: EIC Yellow Report. (2021). [arXiv:2103.0541](https://arxiv.org/abs/2103.0541).
- [8] U. Holm, The ZEUS detector: Status report 1993.
<http://dx.doi.org/10.3204/PUBDB-2017-12635>, 1993.
- [9] H. Abramowicz, A. Caldwell and R. Sinkus, Neural network based electron identification in the ZEUS calorimeter. Nucl. Instrum. Meth. **A365**, 508 (1995). [arXiv:hep-ex/9505004](https://arxiv.org/abs/hep-ex/9505004).
- [10] A. Accardi et al., Electron Ion Collider: The Next QCD Frontier. Eur. Phys. J. **A52**, 268 (2016). [arXiv:1212.1701](https://arxiv.org/abs/1212.1701).
- [11] Junze Liu et al., Deep-Learning-Based Kinematic Reconstruction for DUNE. (2020). [arXiv:2012.0618](https://arxiv.org/abs/2012.0618).
- [12] A. Kwiatkowski, H. Spiesberger and H.J. Moring, Heracles: An Event Generator for ep Interactions at HERA Energies Including Radiative Processes: Version 1.0. Comput. Phys. Commun. **69**, 155 (1992).
- [13] G. Altarelli and G. Parisi, Asymptotic Freedom in Parton Language. Nucl. Phys. **B126**, 298 (1977).
- [14] T. Sjöstrand, S. Mrenna and P.Z. Skands, PYTHIA 6.4 physics and manual. JHEP **05**, 026 (2006). [arXiv:hep-ph/0603175](https://arxiv.org/abs/hep-ph/0603175).

- [15] T. Sjöstrand et al., An introduction to PYTHIA 8.2. *Comput. Phys. Commun.* **191**, 159 (2015). [arXiv:1410.3012](#).
- [16] Sherpa Coll., E. Bothmann et al., Event generation with SHERPA 2.2. *SciPost Phys.* **7**, 034 (2019). [arXiv:1905.0912](#).
- [17] W. Kilian, T. Ohl and J. Reuter, WHIZARD: Simulating Multi-Particle Processes at LHC and ILC. *Eur. Phys. J.* **C71**, 1742 (2011). [arXiv:0708.4233](#).
- [18] J. Bellm et al., Herwig 7.0/Herwig++ 3.0 release note. *Eur. Phys. J.* **C76**, 196 (2016). [arXiv:1512.0117](#).
- [19] G. Ingelman, A. Edin and J. Rathsman, LEPTO 6.5: A Monte Carlo generator for deep inelastic lepton - nucleon scattering. *Comput. Phys. Commun.* **101**, 108 (1997). [arXiv:hep-ph/9605286](#).
- [20] L. Lönnblad, ARIADNE version 4: a program for simulation of QCD cascades implementing the color dipole model. *Comput. Phys. Commun.* **71**, 15 (1992).
- [21] H. Jung et al., The CCFM Monte Carlo generator CASCADE version 2.2.03. *Eur. Phys. J.* **C70**, 1237 (2010). [arXiv:1008.0152](#).
- [22] H. Jung, Hard diffractive scattering in high-energy ep collisions and the Monte Carlo generator RAPGAP. *Comput. Phys. Commun.* **86**, 147 (1995).
- [23] F. Cascioli, P. Maierhofer and S. Pozzorini, Scattering Amplitudes with OpenLoops. *Phys. Rev. Lett.* **108**, 111601 (2012). [arXiv:1111.5206](#).
- [24] Z. Bern et al., The BlackHat library for one-loop amplitudes. *J. Phys. Conf. Ser.* **523**, 012051 (2014). [arXiv:1310.2808](#).
- [25] J. Alwall et al., MadGraph 5 : Going Beyond. *JHEP* **06**, 128 (2011). [arXiv:1106.0522](#).
- [26] R. Brun et al., GEANT3.
<https://cds.cern.ch/record/1119728/files/CERN-DD-EE-84-1.pdf>, 1987.
- [27] GEANT4 Coll., S. Agostinelli et al., GEANT4—a simulation toolkit. *Nucl. Instrum. Meth.* **A506**, 250 (2003).
- [28] S. Bentvelsen, J. Engelen and P. Kooijman, Reconstruction of (x, Q^2) and extraction of structure functions in neutral current scattering at HERA, Workshop on Physics at HERA Hamburg, Germany, October 29-30, 1991, pp. 23–42. (1992).
- [29] A. Arbuzov et al., Hector 1.00: A Program for the calculation of QED, QCD and electroweak corrections to ep and $lepton^\pm N$ deep inelastic neutral and charged current scattering. *Comput. Phys. Commun.* **94**, 128 (1996). [arXiv:hep-ph/9511434](#).

- [30] ZEUS Coll., J. Malka and K. Wichmann, The ZEUS data preservation project. *J. Phys. Conf. Ser.* **396**, 022033 (2012).
- [31] ZEUS Coll., A. Verbytskyi, The ZEUS long term data preservation project. *PoS DIS2016*, 264 (2016). [arXiv:1607.0189](#).
- [32] K. He et al., Deep Residual Learning for Image Recognition. (2015). [arXiv:1512.0338](#).
- [33] A. Farhat, Foundations of deep learning and applications to nuclear physics, Ph.D. thesis, Old Dominion University, in preparation.
- [34] K. Hornik, M. Stinchcombe and H. White, Multilayer feedforward networks are universal approximators. *Neural Networks* **2**, 359 (1989).
- [35] E. Candes, J. Romberg and T. Tao, Robust Uncertainty Principles : Exact Signal Frequency Information. *IEEE Transactions on Information Theory* **52**, 489 (2006).
- [36] H. Zhang, Y. Xu and J. Zhang, Reproducing kernel Banach spaces for machine learning. *Journal of Machine Learning Research*, p. 2741 (2009).
- [37] D.P. Bertsekas and J. Tsitsiklis, Gradient convergence in gradient methods with errors. *SIAM Journal on Optimization* **10**, 627 (2000).
- [38] I. Sutskever et al., On the importance of initialization and momentum in deep learning. *ICML'13: Proceedings of the 30th International Conference on International Conference on Machine Learning* **28**, 1139–1147 (2013).
- [39] A. Krizhevsky et al., ImageNet Classification with Deep Convolutional Neural Networks, in *Advances in Neural Information Processing Systems 25*, eds. F. Pereira and C. J. C. Burges and L. Bottou and K. Q. Weinberger, pp. 1097–1105. Curran Associates, Inc., 2012.
- [40] CTEQ Coll., H.L. Lai et al., Global QCD analysis of parton structure of the nucleon: CTEQ5 parton distributions. *Eur. Phys. J.* **C12**, 375 (2000). [arXiv:hep-ph/9903282](#).
- [41] M. Bengtsson and T. Sjostrand, Parton Showers in Leptoproduction Events. *Z. Phys.* **C37**, 465 (1988).
- [42] G. Gustafson and U. Pettersson, Dipole Formulation of QCD Cascades. *Nucl. Phys.* **B306**, 746 (1988).
- [43] I. Antcheva et al., ROOT: A C++ framework for petabyte data storage, statistical analysis and visualization. *Comput. Phys. Commun.* **182**, 1384 (2011).
- [44] ZEUS Coll., J. Breitweg et al., Measurement of high Q^2 neutral current e^+p deep inelastic scattering cross-sections at HERA. *Eur. Phys. J.* **C11**, 427 (1999). [arXiv:hep-ex/9905032](#).

- [45] ZEUS Coll., S. Chekanov et al., Jet-radius dependence of inclusive-jet cross-sections in deep inelastic scattering at HERA. *Phys. Lett.* **B649**, 12 (2007).
[arXiv:hep-ex/0701039](https://arxiv.org/abs/hep-ex/0701039).
- [46] ZEUS Coll., S. Chekanov et al., Event shapes in deep inelastic scattering at HERA. *Nucl. Phys.* **B767**, 1 (2007). [arXiv:hep-ex/0604032](https://arxiv.org/abs/hep-ex/0604032).
- [47] ZEUS Coll., S. Chekanov et al., Inclusive-jet and dijet cross-sections in deep inelastic scattering at HERA. *Nucl. Phys.* **B765**, 1 (2007). [arXiv:hep-ex/0608048](https://arxiv.org/abs/hep-ex/0608048).
- [48] ZEUS Coll., H. Abramowicz et al., Inclusive-jet cross sections in NC DIS at HERA and a comparison of the kT, anti-kT and SIScone jet algorithms. *Phys. Lett.* **B691**, 127 (2010). [arXiv:1003.2923](https://arxiv.org/abs/1003.2923).
- [49] ZEUS Coll., H. Abramowicz et al., Inclusive dijet cross sections in neutral current deep inelastic scattering at HERA. *Eur. Phys. J.* **C70**, 965 (2010).
[arXiv:1010.6167](https://arxiv.org/abs/1010.6167).
- [50] D. Lontkovskiy, Measurement of Jet Production with the ZEUS Detector, Ph.D. thesis, Hamburg U., 2015. [Http://ediss.sub.uni-hamburg.de/volltexte/2016/7801/](http://ediss.sub.uni-hamburg.de/volltexte/2016/7801/).
- [51] H. Perrey, Jets at low Q^2 at HERA and radiation damage studies for silicon sensors for the XFEL, Ph.D. thesis, Hamburg U., 2011. <http://www-library.desy.de/preparch/desy/thesis/desy-thesis-11-021.pdf>.
- [52] S. Smith, P. Kindermans and Q. Le, Don't Decay the Learning Rate, Increase the Batch Size. (2017). [arXiv:1711.0048](https://arxiv.org/abs/1711.0048).
- [53] R. Aggarwal, Measurement of high x neutral current ep cross sections and extractions of $x F^3$ structure function using ZEUS detector at HERA, Ph.D. thesis, Panjab University, 2012. [Http://hdl.handle.net/10603/80282](http://hdl.handle.net/10603/80282).
- [54] W. McKinney, Data Structures for Statistical Computing in Python, Proceedings of the 9th Python in Science Conference, Stéfan van der Walt and Jarrod Millman (eds.), pp. 56 – 61. (2010), doi:10.25080/Majora-92bf1922-00a.
- [55] F. Chollet et al., Keras. <https://keras.io>, 2015.
- [56] M. Abadi et al., TensorFlow: Large-Scale Machine Learning on Heterogeneous Systems. <http://tensorflow.org/>, 2015.
- [57] G. Guennebaud, B. Jacob et al., Eigen v3. <http://eigen.tuxfamily.org>, 2021.
- [58] T. Hermann, frugally-deep. <https://github.com/Dobiasd/frugally-deep>, 2021.
- [59] T. Hermann, FunctionalPlus. <https://github.com/Dobiasd/FunctionalPlus>, 2021.
- [60] N. Lohmann, JSON for Modern C++ . <https://github.com/nlohmann/json>, 2021.

- [61] NVIDIA Corp., P. Vingelmann and F.H.P Fitzek, CUDA, release: 10.2.89.
<https://developer.nvidia.com/cuda-toolkit>, 2020.
- [62] Max-Planck Computing and Data Facility, About the HPC system Cobra.
<https://www.mpcdf.mpg.de/services/supercomputing/cobra>, 2021.
- [63] R.M. Stallman and GCC Developer Community, Using The Gnu Compiler Collection: A Gnu Manual For GCC Version 4.3.3. CreateSpace, Paramount, CA, 2009.
- [64] Python Software Foundation, Python Language Reference, version 3.
<http://www.python.org>, 2019.
- [65] C. Feuersänger, PGFPlots. <http://pgfplots.sourceforge.net/>, 2021.